

# Tin Gallium Oxide Epilayers on Different Substrates: Optical and Compositional Analysis

Daniel. A. Hunter,\* Gunasekar Naresh-Kumar, Paul R. Edwards, Olha Makydonska, Fabien C. P. Massabuau, Isa Hatipoglu, Partha Mukhopadhyay, Winston V. Schoenfeld, and Robert W. Martin

Electron beam techniques have been used to analyze the impact of substrate choice and growth parameters on the compositional and optical properties of tin gallium oxide  $[(\text{Sn}_x\text{Ga}_{1-x})_2\text{O}_3]$  thin films grown by plasma-assisted molecular beam epitaxy. Sn incorporation and film quality are found to be highly dependent on growth temperature and substrate material (silicon, sapphire, and bulk  $\text{Ga}_2\text{O}_3$ ) with alloy concentrations varying up to an  $x$  value of 0.11. Room temperature cathodoluminescence spectra show the Sn alloying suppressing UV (3.3–3.0 eV), enhancing blue (2.8–2.4 eV), and generating green (2.4–2.0 eV) emission, indicative of the introduction of a high density of gallium vacancies ( $V_{\text{Ga}}$ ) and subsequent  $V_{\text{Ga}}\text{-Sn}$  complexes. This behavior was further analyzed by mapping composition and luminescence across a cross section. Compared to  $\text{Ga}_2\text{O}_3$ , the spectral bands show a clear redshift due to bandgap reduction, confirmed by optical transmission measurements. The results show promise that the bandgap of gallium oxide can successfully be reduced through Sn alloying and used for bandgap engineering within UV optoelectronic devices.

( $\alpha$ -) polymorphs have bandgaps of ( $E_g \approx 4.8$  eV)<sup>[1]</sup> and ( $\approx 5.1\text{--}5.3$  eV),<sup>[2]</sup> respectively. These bandgaps allow these materials to operate as photodetectors within the UV-C energy range making them prime candidates for future solar-blind photodetectors to be used within missile detection and guidance,<sup>[3]</sup> flame detection,<sup>[4]</sup> the monitoring of ozone layer damage,<sup>[5]</sup> and modern non-line of sight UV communication systems<sup>[6,7]</sup> including underwater communication.<sup>[8]</sup> The large breakdown field of the material ( $\approx 8$  MeV  $\text{cm}^{-1}$ ) also makes the material suitable for high-power electronics and energy transmission<sup>[9,10]</sup>

Other ultra wide-gap semiconductor materials such as III-nitrides (e.g., AlGaIn) have been shown to be capable of producing acceptable photodetectors.<sup>[11,12]</sup> However,  $\text{Ga}_2\text{O}_3$ -based detectors benefit from ultra high responsivity<sup>[13]</sup> with the added advantage of the availability of large area, single crystal  $\text{Ga}_2\text{O}_3$  substrates, allowing the growth of near lattice-matched epilayers.  $\beta\text{-Ga}_2\text{O}_3$  also possesses a higher breakdown voltage than GaN, due to the larger bandgap, making it more desirable for high-power applications.


A key benefit of using III-nitride materials is the ability to tune the material bandgap by producing ternary alloys with a

## 1. Introduction

Gallium oxide ( $\text{Ga}_2\text{O}_3$ ) is an ultra wide-bandgap semiconductor currently undergoing a rapid technological maturation for uses within high-power electronics and optical devices. The thermodynamically stable monoclinic ( $\beta$ -) and the metastable corundum

D. A. Hunter, G. Naresh-Kumar, P. R. Edwards, O. Makydonska, F. C. P. Massabuau, R. W. Martin  
Department of Physics  
SUPA  
University of Strathclyde  
Glasgow G4 0NG, UK  
E-mail: daniel.alasdair.hunter@gmail.com

G. Naresh-Kumar  
School of Physics and Astronomy  
Cardiff University  
Cardiff CF24 3AA, UK

 The ORCID identification number(s) for the author(s) of this article can be found under <https://doi.org/10.1002/pssb.202400137>.

© 2024 The Author(s). physica status solidi (b) basic solid state physics published by Wiley-VCH GmbH. This is an open access article under the terms of the Creative Commons Attribution License, which permits use, distribution and reproduction in any medium, provided the original work is properly cited.

DOI: 10.1002/pssb.202400137

I. Hatipoglu  
Photonics Application and Research Center  
Gazi University  
Ankara 06500, Turkey

I. Hatipoglu  
Department of Photonics  
Faculty of Applied Sciences  
Gazi University  
Ankara 06500, Turkey

I. Hatipoglu, P. Mukhopadhyay, W. V. Schoenfeld  
CREOL  
The College of Optics and Photonics  
University of Central Florida  
Orlando, FL 32816, USA

compositional-dependant bandgap, thereby opening the path to heterostructures and bandgap engineering. The same principle can be applied to Ga<sub>2</sub>O<sub>3</sub>, alloying with Al<sub>2</sub>O<sub>3</sub> to increase the bandgap or In<sub>2</sub>O<sub>3</sub> to decrease it.<sup>[14]</sup> Films of high-quality Ga<sub>2</sub>O<sub>3</sub> and subsequent ternary alloys [e.g., aluminum gallium oxide (AGO) and indium gallium oxide (IGO)] have previously been grown on a range of substrates through a variety of growth techniques.<sup>[14–18]</sup> IGO films have been grown over a large range of In/Ga compositions using pulsed laser deposition (PLD), reducing the bandgap by up to 1 eV.<sup>[14]</sup> As the In/Ga ratio is increased above ≈0.3, the IGO begins to form a mixed crystallographic state (monoclinic–hexagonal–cubic) with a high defect concentration and poor crystal quality, impacting the device capabilities of these materials, and it is therefore important to investigate alternative alloys. Rather than alloying with In<sub>2</sub>O<sub>3</sub>, we have taken the alternative approach of alloying with tin oxide (SnO<sub>2</sub> E<sub>g</sub> ≈ 3.6 eV), forming a tin-gallium oxide (TGO, (Sn<sub>x</sub>Ga<sub>1-x</sub>)<sub>2</sub>O<sub>3</sub>) alloy with the aim of producing a tunable lower bandgap material compatible with Ga<sub>2</sub>O<sub>3</sub>.

Sn has been commonly used as a dopant in β-Ga<sub>2</sub>O<sub>3</sub> to produce n-type conductivity within the material,<sup>[19]</sup> but little is known about material properties when the Sn content is increased to alloying levels. Here we present a study characterizing the optical and compositional properties of a series of TGO thin films grown by plasma-assisted molecular beam epitaxy (MBE) on various substrates, namely (010) and (-201) bulk Sn-doped Ga<sub>2</sub>O<sub>3</sub> produced by edge-defined film-fed growth (EFG),<sup>[20]</sup> (0001) sapphire, and (111) silicon. TGO films have previously been grown using the sol–gel process<sup>[21]</sup> and atomic layer deposition<sup>[22]</sup> over a large composition range; however, both growth techniques result in limited crystal quality. Their optical transmission spectroscopy measurements indicate a bandgap reduction of ≈0.5–0.6 eV with Sn contents of  $x \approx 0.2$ –0.25, where  $x$  indicates the Sn content in the formula (Sn<sub>x</sub>Ga<sub>1-x</sub>)<sub>2</sub>O<sub>3</sub>. Ref.[23] showed that PLD from a sintered mixture of Ga<sub>2</sub>O<sub>3</sub> and SnO<sub>2</sub> can be used to produce TGO photodetectors ( $x = 0.1$ ) with significantly increased photocurrent and enhanced responsivity compared to a Ga<sub>2</sub>O<sub>3</sub>-based device and show similar redshifts in the optical bandgap of ≈0.1 and 0.45 eV for Sn contents of  $x = 0.1$  and 0.3, respectively. CVD has been shown to be capable of growing TGO films displaying similar device characteristics as PLD-grown material.<sup>[24]</sup> Here we report on investigations of the compositional and luminescence of a range of MBE-grown TGO films, with their device properties reported elsewhere.<sup>[13,25–27]</sup> The key objective of this work is to show how different substrates with similar growth settings differ in terms of composition and growth rate. It is preferable to grow an alloy of Ga<sub>2</sub>O<sub>3</sub> on its native substrate. Therefore, we have chosen the two most commonly used orientations of Ga<sub>2</sub>O<sub>3</sub>, that is, (-201), and (010). However, Ga<sub>2</sub>O<sub>3</sub> substrates are expensive, which motivates the heteroepitaxial growth of TGO on more cost-effective Si and sapphire. Si substrates offer the advantage of facilitating monolithic integration with Si electronics expanding the potential applications of TGO films and sapphire substrates were selected based on the successful achievement of high-quality Ga<sub>2</sub>O<sub>3</sub> films on this substrate material.

We have analyzed multiple TGO samples using the electron microscopy techniques of wavelength dispersive X-ray (WDX) spectroscopy and cathodoluminescence (CL) spectroscopy/

imaging. The WDX determines the elemental composition allowing us to investigate how variations in the growth conditions impact the extent of Sn incorporation, and the CL data give details of the optical properties measured at the same micron-scale regions.

## 2. Experimental Section

TGO epilayers were grown using plasma-assisted MBE on (010) and (-201) bulk single crystal Ga<sub>2</sub>O<sub>3</sub>, (0001) sapphire, and (111) silicon. Knudsen effusion cells acted as the tin and gallium sources, whereas oxygen was supplied by an SVT Associates plasma source. Surface contamination was removed from the substrate prior to the growth stage through high-temperature annealing (780–800 °C) and through etching with dilute HF followed by rinsing with de-ionized water. A thin Ga<sub>2</sub>O<sub>3</sub> nucleation layer was used in all sapphire substrate samples and one Si sample, as identified with a (\*) in Table 1. The Ga<sub>2</sub>O<sub>3</sub> nucleation layer was grown at a low temperature (500 °C) with a growth time of 5 min, oxygen flow rate of 1.6 SCCM, and plasma power of 300 W. The TGO films were then grown at 600 °C for the Si (010) and (-201) Ga<sub>2</sub>O<sub>3</sub> substrates, while a reduced temperature of 500 °C was used for the sapphire substrate (to match the growth temperature of the nucleation layer required to improve sample quality). A standard oxygen flow rate and plasma power of 2.5 sccm and 300 W were used for all samples with the amount of Sn and Ga available during the growth varied by altering the effusion cell temperature. The growth parameters and compositional details of each sample are given in Table 1. The thickness of the films on the various substrates varied between 0.125 and 1.25 μm. (see Table 1). The growth rates for the TGO films (see Table 1) vary considerably for the different substrates. The low growth rate for the samples on sapphire is largely due to the reduced growth temperature, but there is still a doubling of growth rate for the layers on Si compared to those on (010) Ga<sub>2</sub>O<sub>3</sub>. The rate is clearly impacted by the strain and crystal orientation of the growing layer as well as the flux rates, substrate temperature, and source temperatures. Cross-sectional secondary electron (SE) imaging was performed to confirm the TGO film thicknesses. X-ray diffraction (XRD) was performed using a PANalytical X'Pert Cu- $\alpha$ 1 beam ( $\lambda = 1.5405 \text{ \AA}$ ).

The WDX and CL measurements were performed on a JEOL JXA-8530 F electron probe microanalyser (EPMA). A 40 nA beam current and 10 μm spot size were used for all WDX measurements. The differences in film thicknesses (Table 1) merited the use of different beam voltages, in order to maximize the Sn X-ray emission. CASINO Monte Carlo simulations<sup>[28]</sup> indicate that using 6 kV for β-Ga<sub>2</sub>O<sub>3</sub> ( $\rho = 5.88 \text{ g cm}^{-3}$ ) results in 90% of the beam energy being deposited within a depth of <175 nm. This was therefore a suitable beam voltage to contain excitation in the TGO film for most samples; however, a reduced beam voltage of 5 kV was required for the sapphire substrate samples (90% of the beam energy deposited within <125 nm). Note that the alloying with Sn increases the film density from 5.88 g cm<sup>-3</sup> toward the SnO<sub>2</sub> density ( $\rho \approx 6.95 \text{ g cm}^{-3}$ ), although only slightly ( $\rho \approx 6$ –6.2 g cm<sup>-3</sup>) for the moderate levels of Sn alloying ( $x < 0.11$ ). Therefore, by performing the calculation for Ga<sub>2</sub>O<sub>3</sub>, we slightly underestimate the real density of the film, and

**Table 1.** Summary of growth conditions, sample properties, and WDX compositional results for all TGO samples. Samples featuring a Ga<sub>2</sub>O<sub>3</sub> nucleation layer are identified with a (\*).

Substrate	$T_{\text{Growth}}$ [°C]	$T_{\text{Ga}}$ [°C]	$T_{\text{Sn}}$ [°C]	Approx. film thickness [μm]	Growth rate [nm h <sup>-1</sup> ]	WDX Total wt%	x [%]
(010)-Sn doped Ga <sub>2</sub> O <sub>3</sub>	600	1000	690	0.25	80–90	101.2	0.2
(010)-Sn doped Ga <sub>2</sub> O <sub>3</sub>	600	1000	750			100.2	5.6
(010)-Sn doped Ga <sub>2</sub> O <sub>3</sub>	600	1000	660			101.8	0.2
(010)-Sn doped Ga <sub>2</sub> O <sub>3</sub>	600	1000	780			101.6	6.1
(-201)-Sn doped Ga <sub>2</sub> O <sub>3</sub>	600	980	830	0.50	120	100.8	2.7
(-201)-Sn doped Ga <sub>2</sub> O <sub>3</sub>	600	980	800			100.8	2.6
(-201)-Sn doped Ga <sub>2</sub> O <sub>3</sub>	600	980	800			101.1	2.4
(-201)-Sn doped Ga <sub>2</sub> O <sub>3</sub>	600	1000	835			101.8	2.1
(111) Si n-type	600	1000	810	1.25	180	97.3	2.2
(111) Si n-type*	600	1000	795			102.7	2.1
(0001) Sapphire*	500	900	730	0.125	25–35	95.9	10.8
(0001) Sapphire*	500	900	750			98.6	11.0
(0001) Sapphire*	500	900	800			97.4	11.1

overestimate the size of the interaction volume, ensuring X-ray generation remained only within the TGO film.

X-ray counting times of 60 s (peak)/30 s (backgrounds) were used for all measurements. The  $k$ -ratios used to determine the material compositions were calculated using the following standards: cassiterite (SnO<sub>2</sub>) for Sn and unintentionally doped bulk Ga<sub>2</sub>O<sub>3</sub> for Ga and O. A thallium acid phthalate (TAP) crystal was used for the Ga  $L_{\alpha}$  and Sn  $L_{\alpha}$  X-rays, while a synthetic layered pseudo-crystal was required for the O  $K_{\alpha}$  X-rays.<sup>[29]</sup> For each sample, multiple measurement points (minimum of 9 per sample) were taken with 0.25–0.5 mm spacing and averaged to determine the material composition. The random error from these measurements was found to be negligible (<0.1%). There is also a systematic uncertainty, estimated to be about 2%,<sup>[30]</sup> due to multiple factors such as differences between the cassiterite standard and the TGO film, differences in surface contamination (especially impacting low energy measurements), and less well-known matrix corrections for non  $K_{\alpha}$  X-rays.

RT CL spectra were acquired using a focussed electron beam with the same beam conditions as the WDX measurements.<sup>[31]</sup> The CL signal was collected using a built-in reflecting objective, focused into an optical fibre with 105 μm optical diameter which was then coupled into an Andor Shamrock 163 spectrometer with a focal length of 163 mm. The dispersed light was then detected using an Andor 1600-channel electron-multiplying charge-coupled device. The spectrometer used for these measurements was equipped with a 300 lines mm<sup>-1</sup> grating blazed at 500 nm. All CL measurements within this manuscript are corrected for system response, which drops off in the UV.

### 3. Results and Discussion

The structural properties of the grown films were investigated using X-Ray diffraction (XRD). Detailed analysis of the XRD data is given elsewhere.<sup>[13,25-27]</sup> Here we show a representative XRD plot (see **Figure 1**) for a TGO sample grown on Si ( $x = 2.23\%$ ),

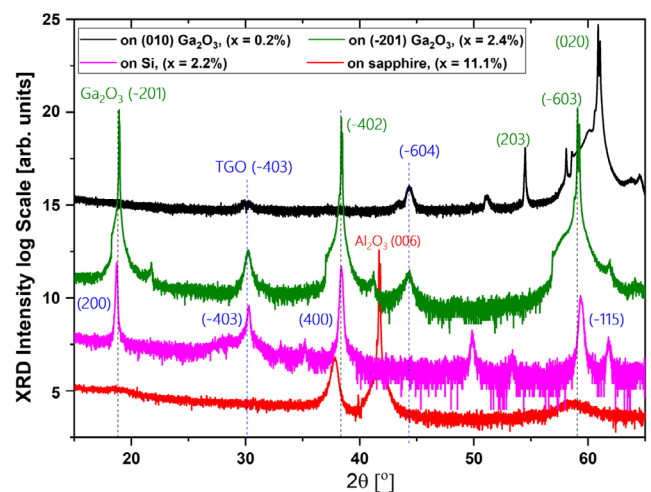


**Figure 1.** Representative XRD plots for TGO films grown on different substrates. TGO grown on (010) Ga<sub>2</sub>O<sub>3</sub> substrate ( $x = 0.2\%$ , black trace), (-201) Ga<sub>2</sub>O<sub>3</sub> substrate ( $x = 2.4\%$ , green trace), Si ( $x = 2.2\%$ , purple trace), and sapphire ( $x = 11.1\%$ , red trace). Detailed analysis of the XRD data is given elsewhere.<sup>[13,25–27]</sup>

sapphire ( $x = 11.14\%$ ), (010) Ga<sub>2</sub>O<sub>3</sub> substrate ( $x = 0.25\%$ ), and (-201) Ga<sub>2</sub>O<sub>3</sub> substrate ( $x = 2.42\%$ ), albeit that it is not possible to have the same Sn content in each case. The pan-analytical XRD database<sup>[32]</sup> is used to index the XRD peaks. As there is a limited XRD database for TGO, we were able to compare our results only to the Ga<sub>4</sub>SnO<sub>8</sub> phase (pdf card no 00-041-0240). The TGO epilayers grown on the (-201) Ga<sub>2</sub>O<sub>3</sub> substrate show two peaks at  $\approx 30.28^\circ$  and  $\approx 44.37^\circ$ , assigned to (-403) and (-604) planes of TGO, whereas the films grown on (010) Ga<sub>2</sub>O<sub>3</sub> substrate show additional peaks at  $\approx 54.50^\circ$ ,  $\approx 59.15^\circ$ , and  $\approx 60.91^\circ$ . These peaks appear to correspond to the (203), (-603), and (020) planes of the Ga<sub>2</sub>O<sub>3</sub> substrate. Considering the slightly broader nature of the additional peak at  $\approx 51.10^\circ$ , it is less likely to be from the Ga<sub>2</sub>O<sub>3</sub>

substrate but likely to be from the TGO film. However, we could not index this peak to the available XRD database.

It is worth noting that the peak position of the (200) plane of TGO is close to the (-201) plane of  $\beta$ - $\text{Ga}_2\text{O}_3$ . Previous reports on MBE growth of  $\text{Ga}_2\text{O}_3$  ( $x = 0\%$ ) on sapphire substrate<sup>[33]</sup> have shown that the XRD peak at  $\approx 19^\circ$  is from the (-201) plane of  $\beta$ - $\text{Ga}_2\text{O}_3$ ; in our case, this peak becomes broader and weaker on increasing the Sn content (e.g., see the red trace in Figure 1 for  $x = 11.4\%$ ). This peak broadening can be attributed to reduced crystal quality of the TGO films or the formation of (200) planes of TGO overlapping with the (-201) plane of  $\beta$ - $\text{Ga}_2\text{O}_3$ . The peak at  $\approx 38^\circ$  which matches the position of the (-402) peak of the  $\beta$ -phase  $\text{Ga}_2\text{O}_3$  also overlaps that of the (0006) peak of  $\alpha$  phase and the (004) peak of  $\kappa$  phase  $\text{Ga}_2\text{O}_3$ .<sup>[34]</sup> The lack of appreciable peak broadening for this peak suggests the presence of another crystal phase in the TGO on sapphire samples with  $x > 10\%$ , most likely the  $\alpha$  phase. Oshima et al.<sup>[35]</sup> have demonstrated that the MBE growth temperatures below  $800^\circ\text{C}$  on sapphire can result in the formation of  $\alpha$ -phase  $\text{Ga}_2\text{O}_3$  along with the  $\beta$  phase, with further lowering of the growth temperature increasing the fraction of the  $\alpha$ -phase.

The TGO film grown on a Si substrate shows a polycrystalline nature due to the large lattice and thermal mismatch between the thin film and the Si substrate. Several peaks were seen, and the most prominent were noted to be (200), (-403), (400), and (-115) planes of TGO.<sup>[27]</sup> Previous literature studies of  $\text{Ga}_2\text{O}_3$  thin films and nanostructures grown on Si substrates<sup>[36,37]</sup> have shown the (-201) and (-402) planes of  $\beta$ - $\text{Ga}_2\text{O}_3$  which are close to the (200) and (400) planes of TGO as shown in this work (see the purple trace in Figure 1). Currently, we could not obtain any direct correlation of the preferred crystal orientations of TGO on Si. However, growing on engineered Si substrates and employing optimized buffer layers may well produce TGO films of preferred crystal orientations.<sup>[38]</sup> Notably, there was no sign of any XRD peaks that correspond to  $\text{SnO}$  or  $\text{SnO}_2$  phases in all our samples (typically around  $24^\circ$ ).

Figure 2 shows an example SE image of the surface of a TGO film for each substrate showing the surface morphology and crystal quality. A fully coalesced TGO film was found for both types of  $\text{Ga}_2\text{O}_3$  substrate and for the sapphire substrate, as shown in Figure 2a–c. As expected, for the phase pure  $\text{Ga}_2\text{O}_3$  epilayer ( $x = 0$ ), the (-201) orientation to the sapphire substrate is preferential since the oxygen atomic arrangement for the (-201) plane for  $\beta$ - $\text{Ga}_2\text{O}_3$  aligns with that of the c-plane sapphire substrate.<sup>[19]</sup> Therefore, it is unsurprising that 2(b) and 2(c) have the best surface/crystal quality, with 2(a) producing a rough(er) film due to growth along a nonpreferential orientation. Earlier studies<sup>[34]</sup> have shown that a tin-enriched surface layer may act as a surfactant aiding the growth of the  $\kappa$  phase. Kracht et al.<sup>[39]</sup> demonstrated that Sn's presence could help attain a metal-rich growth regime in MBE and aid in stabilizing the  $\epsilon$  phase of  $\text{Ga}_2\text{O}_3$ . In our TGO samples, the growth conditions differ from those of refs. [34,39]. Nonetheless, our XRD results indicate the presence of other phases for high Sn-containing samples on sapphire; further work is required to classify their types unambiguously.

The TGO film grown directly upon Si exhibits poor morphology featuring voids surrounding large flake-like structures composing the film, as shown in Figure 2d. The inclusion of the  $\text{Ga}_2\text{O}_3$  buffer layer reduces the occurrence of these voids and the flake structures coalesce into a more complete TGO layer, as shown in Figure 2e.

The impact of the  $\text{Ga}_2\text{O}_3$  buffer layer on the formation of these voids has been confirmed through cross-sectional SE imaging shown in Figure 3. Figure 3a shows a cross section of the TGO/Si film where a large amount of deep voids are present, and Figure 3b, however, shows the formation of a more coalesced TGO film with fewer voids. The voids in Figure 2d pose an issue for the quantification of the TGO composition. These voids may extend to the Si substrate, forming empty channels that allow electron propagation deep within the film and could result in

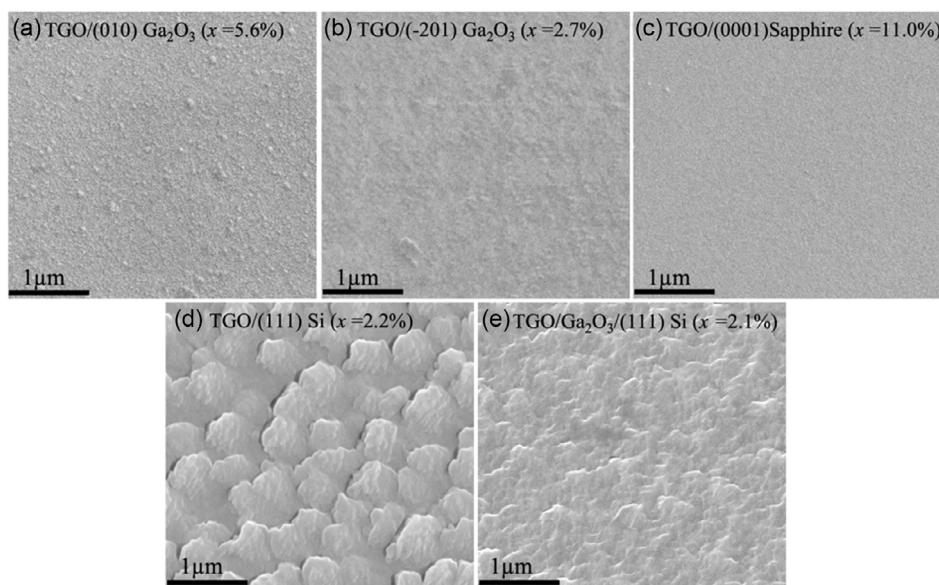


**Figure 2.** Secondary electron images of TGO samples. a) TGO/(010)  $\text{Ga}_2\text{O}_3$  ( $x = 5.6\%$ ), b) TGO/(-201)  $\text{Ga}_2\text{O}_3$  ( $x = 2.7\%$ ), c) TGO/(0001) Sapphire ( $x = 11.0\%$ ), d) TGO/(111) Si ( $x = 2.2\%$ ) and e) TGO/ $\text{Ga}_2\text{O}_3$ /(111) Si ( $x = 2.1\%$ ).

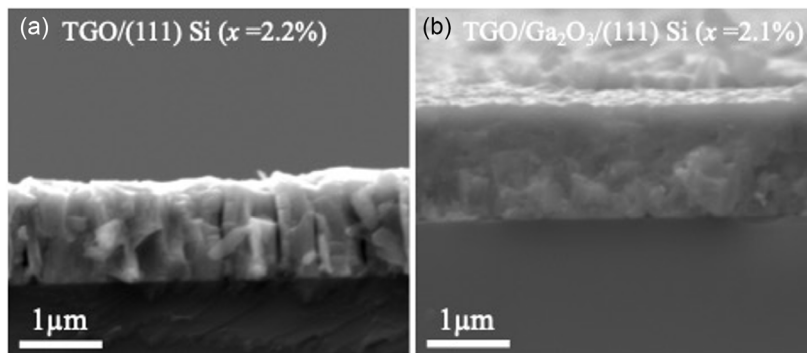


**Figure 3.** Cross-sectional SE images of TGO samples: a) TGO/(111) Si ( $x = 2.2\%$ ) and b) TGO/Ga<sub>2</sub>O<sub>3</sub>/(111) Si ( $x = 2.1\%$ ).

X-ray generation within the Si substrate. The average weight total percentage (wt%) calculated by the WDX measurements (see Table 1) indicates this has had a minimal effect on our composition calculations. The wt%'s for our measurements are all close to 100% providing a high level of confidence in the elemental compositions determined by WDX analysis. The low wt% for the (0001)-sapphire substrate samples is likely due to moderate sample charging caused by the insulating nature of the substrate.

**Figure 4** plots the sample composition determined by WDX against the ratio of the Sn and Ga cell temperatures during the growth process. First, the reduced substrate temperature for the sapphire substrate samples (500 °C, green inverted triangular data points) compared to the other substrates (600 °C) results in significantly higher Sn incorporation. In the case of Ga<sub>2</sub>O<sub>3</sub>:Sn grown by MBE, it has been shown that there is an increase in carrier concentration for crystals grown at lower substrate temperatures (540 °C) compared to higher temperature growth (600 °C).<sup>[40]</sup> While this behavior is seen for much lower Sn concentrations than in our TGO films, this could indicate there is a preferential substrate temperature of  $\approx 500$  °C or less to maximize Sn incorporation within Ga<sub>2</sub>O<sub>3</sub>. However, growth of

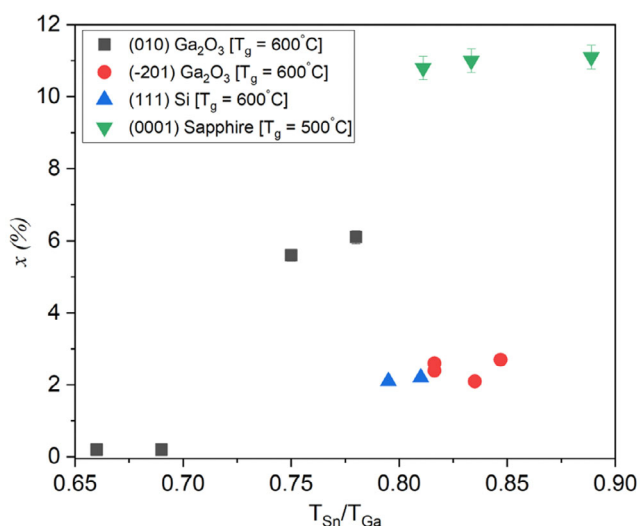


**Figure 4.** (Sn<sub>x</sub>Ga<sub>1-x</sub>)<sub>2</sub>O<sub>3</sub> composition determined by WDX plotted against the temperature ratio of the Sn and Ga effusion cells during the growth process. The different symbols distinguish the different substrates.

Ga<sub>2</sub>O<sub>3</sub> films at lower growth temperature brings additional complications such as poorer crystal and surface quality<sup>[41,42]</sup> and the formation of other polymorphs.<sup>[35]</sup>

Similar Sn incorporation was found for the (-201) Ga<sub>2</sub>O<sub>3</sub> (red circles) and (111) Si (filled blue triangles) substrate samples which share similar growth conditions (see Table 1), but it is noteworthy that there is a much larger level of Sn incorporation for samples with (010) Ga<sub>2</sub>O<sub>3</sub> substrates (black squares) than (-201) ones for lower  $T_{Sn}/T_{Ga}$  ratios. A similar trend has been seen for other more widely studied Ga<sub>2</sub>O<sub>3</sub> alloys: for AGO films grown by MBE on (-201) and (010) Ga<sub>2</sub>O<sub>3</sub> substrates there was a roughly 50% uptake of Al for films grown on (-201) Ga<sub>2</sub>O<sub>3</sub> compared to (010) when grown under the same conditions.<sup>[43]</sup> The  $\beta$ -Ga<sub>2</sub>O<sub>3</sub> crystal structure features two types of Ga sites, octahedral (Ga<sub>II</sub>) and tetrahedral (Ga<sub>I</sub>) which are alternatively exposed in the (-201) growth direction, unlike the (010) direction which features octahedral-only stacking. It has been found that Al has a preference to substitute into the octahedral site, only integrating within the preferred site for (-201) growth.<sup>[16,43,44]</sup> If Sn was to show a similar preference, there would be a greater Sn incorporation for TGO films on (010) Ga<sub>2</sub>O<sub>3</sub> substrates compared to (-201), as seen here. The greater size of the Sn atoms compared to Ga makes the octahedral sites preferential for Sn incorporation within bulk Ga<sub>2</sub>O<sub>3</sub> due to the similarity of the Ga<sub>II</sub>-O (octahedral Ga site) bond length in Ga<sub>2</sub>O<sub>3</sub> (2.02 Å) to Sn-O in SnO<sub>2</sub> (2.2 Å) hence increasing the incorporation for the (010) Ga<sub>2</sub>O<sub>3</sub> substrate.<sup>[45]</sup>

Tetravalent Sn donors (Sn<sup>4+</sup>) in the Ga<sub>II</sub> site tend to generate gallium vacancies to satisfy charge neutrality in the crystal lattice. Our previous work<sup>[13]</sup> pointed to Sn incorporation into the Ga<sub>2</sub>O<sub>3</sub> crystal lattice generating gallium vacancies ( $V_{Ga}$ ), with theoretical support from first principle calculations. While the work of Mi et al.<sup>[46]</sup> shows an increase in conductivity for increasing Sn content, we did not observe any clear correlation between Sn incorporation and conductivity from  $I$ - $V$  characteristics of deep UV photodetectors fabricated from TGO on (-201) Ga<sub>2</sub>O<sub>3</sub> substrates.<sup>[13]</sup> We will also describe observation of clear Sn- $V_{Ga}$ -related emissions in the CL spectroscopy. We conclude it is likely that the Sn is in the tetravalent form (at least in our samples).

There appears to be a correlation between the Sn uptake and film thickness with the thinnest films displaying the largest alloy concentration (see Table 1); however, we believe the two are unrelated. We would expect a Sn composition gradient to be seen if this was the case, with the largest Sn concentration at the

substrate interface which would gradually reduce as the film thickness is increased. Cross-sectional WDX mapping reveals this not to be the case as the TGO films have a near-uniform Sn profile (see below).

**Figure 5** shows the raw and normalized cathodoluminescence spectra obtained from a selection of the TGO films. The sapphire substrate samples showed weak CL and are excluded from this figure. For these samples, the combination of the reduced beam energy and the magnified Sn composition contribute to the quenching of the luminescence (explained in more detail later). Plan-view CL point measurements for the TGO/Si, and TGO/Ga<sub>2</sub>O<sub>3</sub>/Si films were heavily influenced by Fabry–Perot interference fringes, resulting in complex multi-peak CL spectra. Therefore, the spectra from these samples were extracted from cross-section maps.

The samples on Ga<sub>2</sub>O<sub>3</sub> substrates show three main luminescence bands, as typically seen for Ga<sub>2</sub>O<sub>3</sub> luminescence: UV (3.3 eV), blue (2.8 eV), and green (2.4 eV)<sup>[47,48]</sup> with all three bands being visible for the TGO films in Figure 5. UV emission in Ga<sub>2</sub>O<sub>3</sub> is attributed to the recombination of free electrons with self-trapped holes (STHs), an intrinsic defect of β-Ga<sub>2</sub>O<sub>3</sub> due to the non-fully bonding of oxygen on one of the three distinct oxygen-binding sites in the β-Ga<sub>2</sub>O<sub>3</sub> crystal.<sup>[49]</sup> Blue emission is generally attributed to donor–acceptor pair recombination (DAP) with the oxygen vacancies (V<sub>O</sub>) being the donors and gallium vacancies (V<sub>Ga</sub>) acting as the acceptors.<sup>[48]</sup> The source of the green emission is not as well established as the UV and blue but has been attributed to DAP recombination involving extrinsic point defects such as Sn, Si, and Be.<sup>[50,51]</sup>

In Figure 5a, there is a clear decrease in the overall luminescence intensity of the thin films as the level of Sn alloying level is increased, with the greatest intensity being for the TGO/(010) Ga<sub>2</sub>O<sub>3</sub> (x = 0.2%) sample and weakest for the x = 5.6% TGO/(010) Ga<sub>2</sub>O<sub>3</sub> sample. The gradual decrease in intensity with increasing Sn concentration implies that structural dislocations or defect levels lying within the bandgap, either directly from the

incorporation of Sn or induced through the alloying, have increased the number of nonradiative recombination pathways present within the semiconductor. Also accompanying the decrease in overall intensity is a modulation of the peak intensities for the three aforementioned spectral bands, this is more clearly seen in the normalized CL data in Figure 5b. Initial observations from Figure 5b show that for TGO films the peak luminescence occurs within the blue spectral region compared to the UV for Ga<sub>2</sub>O<sub>3</sub>. The quenching of the UV luminescence within the TGO films implies that DAP recombination is now the dominant recombination mechanism. The enhancement of the blue emission suggests the increased presence of V<sub>Ga</sub> induced by the Sn alloying. The green emission is solely found within the TGO films, indicating that this emission is related to the addition of Sn, potentially through vacancy complexes involving Sn or the greater V<sub>Ga</sub> density induced through alloying. Hybrid functional calculations have identified that the formation of Sn-based defects within β-Ga<sub>2</sub>O<sub>3</sub> result in optical transitions between free electrons and V<sub>Ga</sub> and V<sub>Ga</sub>–Sn complexes which have emission energies within these spectral ranges.<sup>[13]</sup> Specifically, free electron recombination with a hole located on the V<sub>Ga</sub><sup>ib</sup> or V<sub>Ga</sub><sup>ic</sup> interstitial Ga sites results in emission energies of 2.69 and 2.56 eV making them possible candidates for the blue emission (there are five distinct interstitial sites in the β-Ga<sub>2</sub>O<sub>3</sub> crystal; V<sub>Ga</sub><sup>ib</sup> and V<sub>Ga</sub><sup>ic</sup> correspond to two of these sites<sup>[52]</sup>). Mechanisms responsible for the green emission may be the recombination of free electrons with holes trapped within the V<sub>Ga(II)</sub> (octahedral Ga vacancy) or the V<sub>Ga(II)</sub>+3Sn complex with emission energies of 2.16 and 2.23 eV, respectively.<sup>[13]</sup> We are confident in the results from these calculations, but there may be other possible explanations for the green emission such as: STH emission occurring from STHs within SnO<sub>2</sub>, with an emission energy calculated to be 2.27 eV;<sup>[53]</sup> transitions involving oxygen interstitials (O<sub>i</sub>)<sup>[54,55]</sup> with the O<sub>i</sub> density greatly increased through the Sn alloying or by transitions directly involving the Sn atoms.<sup>[56]</sup> For the level of alloying in the relevant samples, we would expect Sn to directly substitute for Ga in the Ga<sub>2</sub>O<sub>3</sub> lattice avoiding the

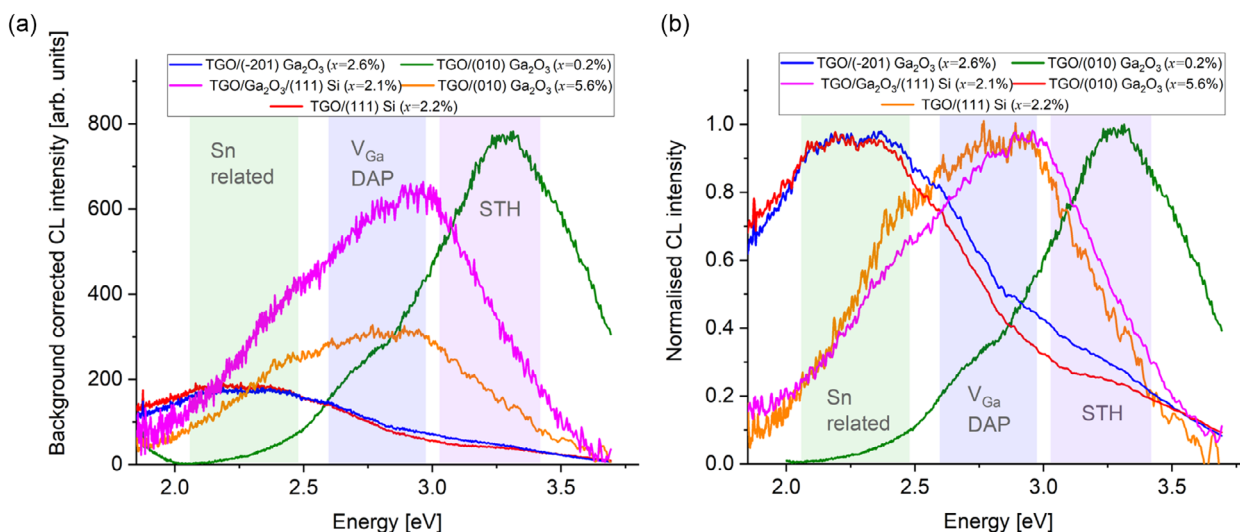


**Figure 5.** Example a) raw and b) normalized CL spectra obtained from TGO films on various substrates: TGO/(010) Ga<sub>2</sub>O<sub>3</sub> with high and low Sn content, TGO/Si, TGO/Ga<sub>2</sub>O<sub>3</sub>/Si, TGO/(-201) Ga<sub>2</sub>O<sub>3</sub> and a (-201) Ga<sub>2</sub>O<sub>3</sub> bulk single crystal. Shading shows the approximate energy of the three spectral bands mentioned in the text.

formation of  $\text{SnO}_2$ . This STH emission from that material would be an unlikely explanation for green emission in our TGO films. The green luminescence in other wide bandgap oxide semiconductors such as ZnO has also been attributed to cation vacancy defect transitions, such as  $V_{\text{Zn}}$ , agreeing with the conclusions here but as stated, similarly to  $\text{Ga}_2\text{O}_3$  there may be multiple sources/factors for this luminescence.<sup>[57,58]</sup> Trace element WDX scans did not identify any bulk impurity elements that may be responsible for the observed emission.

To further correlate the optical behavior with the incorporation of Sn, we have performed combined WDX and CL cross-sectional mapping with both signals simultaneously acquired in one scan. A CL hyperspectral image was collected, and “peak intensity” CL maps were extracted from this dataset by integrating over selected wavelength bands. **Figure 6** shows the results from the mapping measurements on the TGO/ $\text{Ga}_2\text{O}_3$ /Si sample with Sn = 2.1%. The thin  $\text{Ga}_2\text{O}_3$  buffer layer was added to improve the surface quality of the sample. The buffer layer was found to have a minimal effect on the Sn incorporation rate.<sup>[27]</sup> Figure 6a shows a WDX map recording the Sn  $L_\alpha$  X-ray counts, and Figure 6b–d shows the CL maps for the three main spectral bands mentioned previously; b) UV [3.3–3.0 eV], c) blue [2.8–2.4 eV], and d) green [2.4–2.0 eV].

Broad energy ranges are used to account for the redshifting of the peak energies with respect to  $\text{Ga}_2\text{O}_3$ . The three sections of the material are marked above Figure 6b; 1) 2.1% TGO, 2)  $\text{Ga}_2\text{O}_3$  buffer, and 3) Si. First, it can be seen in Figure 6a that the Sn X-ray counts are exclusive to a thin film ( $\approx 1.25 \mu\text{m}$ ) corresponding to the region (1) in Figure 6b. The  $\text{Ga}_2\text{O}_3$  buffer layer [region (2)] cannot be seen in 6(a), but is clearly seen in 6(b) and (c) where the light-emitting cross section is noticeably thicker than in 6(a). CL intensity variations between the two layers also help identify the distinct regions of the cross section. The Si substrate is present in the region (3) but is not highlighted by the signals used in this figure. The UV emission shown in 6(b) can be separated into two distinct zones: a bright UV peak in the  $\text{Ga}_2\text{O}_3$  buffer layer ( $2 \times 10^4$  counts) and a diminished emission within the TGO film ( $1 \times 10^4$  counts). Figure 6c shows the inverse of (b) with the brightest blue emission occurring in the TGO layer ( $2 \times 10^4$  counts), while the  $\text{Ga}_2\text{O}_3$  displays a reduced intensity ( $0.5 \times 10^4$  counts). This reinforces the observation that the UV quenching and blue enhancement seen in Figure 5 are due to the Sn alloying. The green emission seen within the TGO films is shown to be all but eliminated within the  $\text{Ga}_2\text{O}_3$  buffer layer, as shown in 6(d).

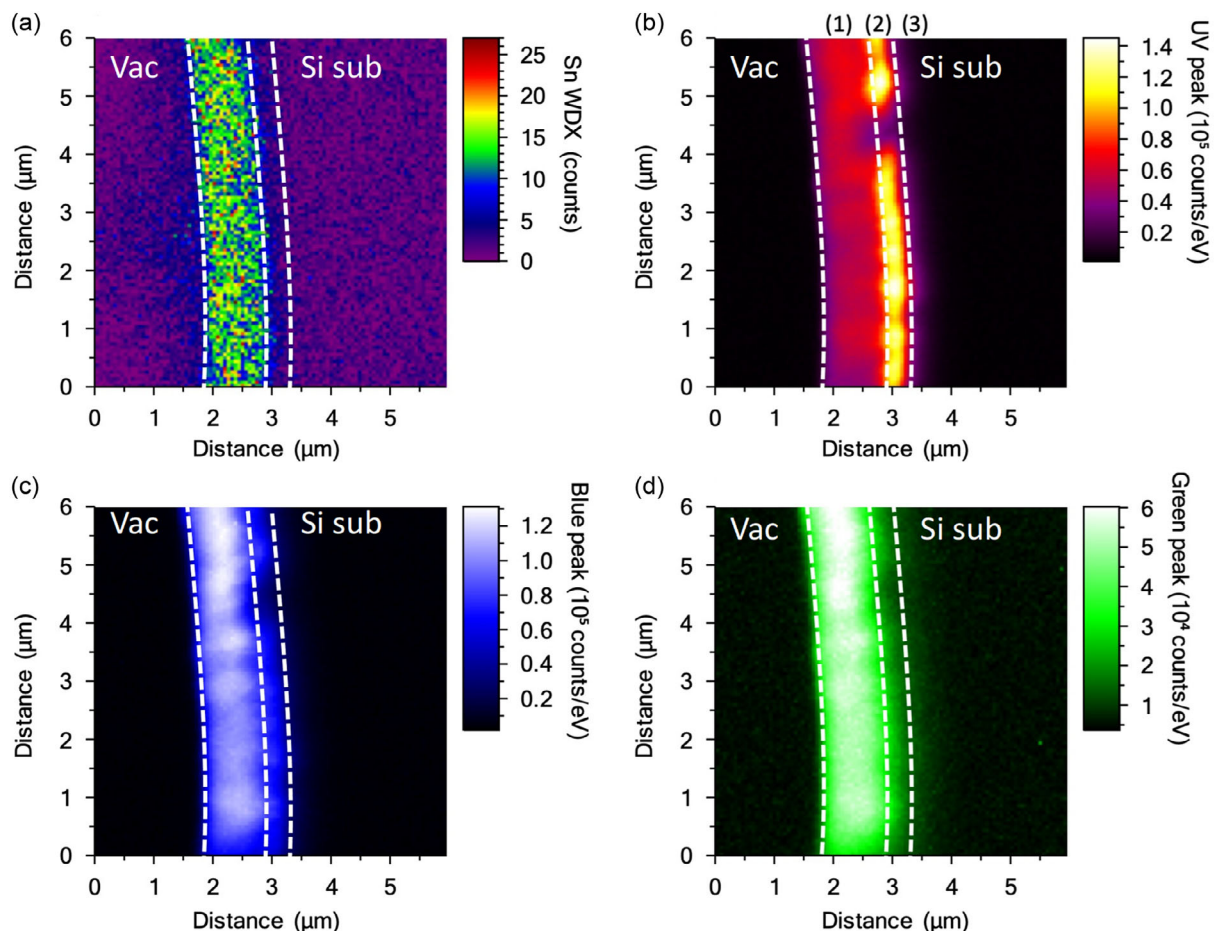


**Figure 6.** Cross-sectional joint WDX and CL maps taken of a TGO/ $\text{Ga}_2\text{O}_3$ /Si sample (Sn = 2.1%). a) Sn  $L_\alpha$  X-ray counts, b–d) peak intensity maps of three spectral regions, specifically b) UV [3.3–3.0 eV], c) blue [2.8–2.4 eV], and d) green [2.4–2.0 eV]. x- and y-axes correspond to the spatial distance over which the cross-sectional map was acquired. Vacuum and substrate side of the cross-section are marked with “Vac” and “Si sub” respectively.

The observation that the green emission is confined to the TGO film agrees with published studies stating that green emission was only present in  $\text{Ga}_2\text{O}_3$  films containing impurities such as  $\text{Sn}^{[50]}$  and reinforces our claim that the green emission originates from DAP recombination involving holes trapped at Sn-induced gallium vacancies,  $V_{\text{Ga}}$ , or free electron recombination involving  $V_{\text{Ga}}\text{-Sn}$  complexes.

As well as the shift in the most intense luminescence from UV to blue with the addition of Sn, there is also a shift of the peak wavelength of the three main spectral bands mentioned above. A deconvolution was performed by fitting to three Gaussian peaks, constraining the peak energies to be within extended energy ranges corresponding to the three observable luminescence peaks, UV [3.4–2.9 eV], (c) blue [2.9–2.4 eV], and (d) green [2.5–1.9 eV]. **Figure 7** plots the deconvolved peak energies for the UV, blue, and green luminescence peaks against the Sn content determined by WDX. Within each band, there is a clear redshifting of the peak, with an Sn content of  $\approx 6\%$  inducing a

redshift of  $\approx 0.3\text{--}0.4\text{ eV}$  for the blue (Figure 7b) and green (Figure 7c) compared to the  $x = 0.2\%$  TGO sample. The shift in UV luminescence, plotted in Figure 7a, is nonlinear with lower Sn contents ( $\approx 2\%$ ) inducing an approximate redshift of  $0.3\text{--}0.4\text{ eV}$  and no further shift for further Sn incorporation ( $\geq 6\%$ ). This nonlinear shift for the UV band could be due to interfering UV emission from an underlying  $\text{Ga}_2\text{O}_3$  layer (either a buffer layer or the  $\text{Ga}_2\text{O}_3$  substrates). The two sources of UV emission may overlap within the CL spectra and cannot be individually deconvolved so the UV peak energy would then be taken from the broadened UV peak and may not identify the “true” redshifted TGO UV emission.

The mechanism causing the redshift of these emission bands cannot be determined with certainty, but multiple factors may be responsible. The reduction of the semiconductor bandgap due to the Sn alloying is the most probable reason for this shift.<sup>[59]</sup> The formation of non- $\beta$ -TGO films is also possible but could not be confirmed using the analytical methods detailed here. Strain is

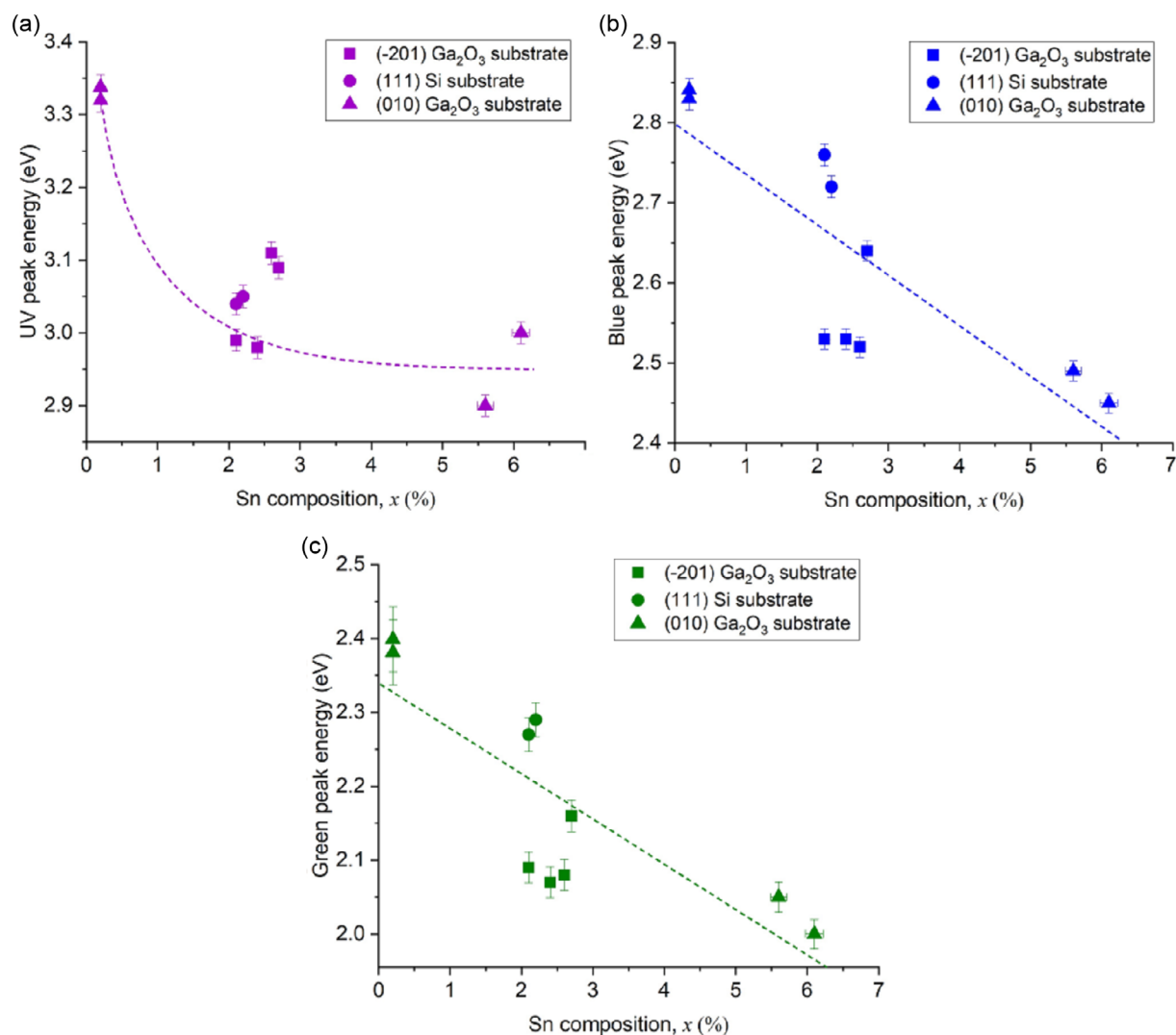


**Figure 7.** Energy of peak emission, determined from the CL, against Sn content for the three main luminescence bands of  $\text{Ga}_2\text{O}_3$ : a) UV, b) blue, and c) green. The lines are guides for the eye.



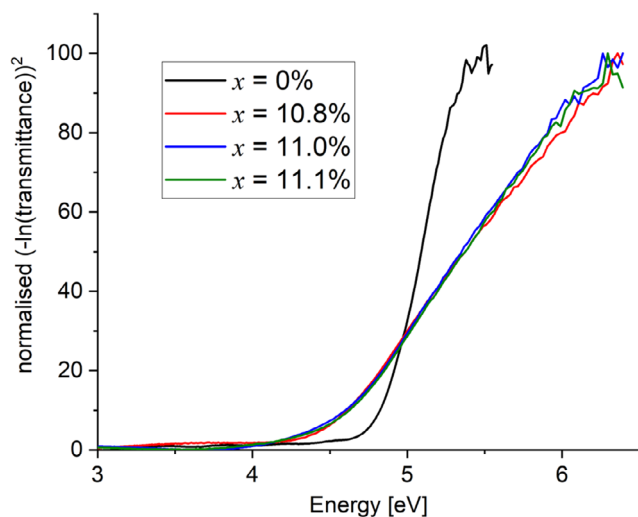


**Figure 8.** Normalized  $(-\ln(\text{transmittance}))^2$  as a function of energy calculated from optical transmission spectroscopy data from the TGO/ $\text{Ga}_2\text{O}_3$ /sapphire samples and an epitaxial  $\text{Ga}_2\text{O}_3$  sapphire reference, indicating the shift in the onset of absorption.

also likely to affect this redshift with a different contribution expected for each substrate. To confirm the shift in bandgap, we have performed optical transmission measurements on the sapphire substrate samples. **Figure 8** plots  $(-\ln(\text{transmittance}))^2$  as a function of energy for the three TGO/sapphire samples and a  $\text{Ga}_2\text{O}_3$ /sapphire reference sample. The reference sample was grown by metal-organic vapor phase epitaxy and has a nominal thickness of 700 nm. The plots are normalized and no account is taken for the reflectivity since different areas of metallization meant that the transmitting area and reflectivity could not be consistent between different samples.

As expected, there is a redshift observed for all three TGO samples compared to a  $\text{Ga}_2\text{O}_3$  reference sample. Due to the similarity in Sn content for the TGO samples, there is little difference in the spectra produced from each. The onset of absorption of these samples has been estimated from the slope of the  $(-\ln(\text{transmittance}))^2$  edge, taking the value to be where the slope intersects the  $x$ -axis. This results in an onset of absorption of 4.49 eV for the  $x = 10.8\%$  and  $x = 11.1\%$  TGO samples, 4.47 eV for  $x = 11.0\%$ , and 4.82 eV for the  $\text{Ga}_2\text{O}_3$  reference ( $x = 0\%$ ). This corresponds to a shift of  $-0.33$  and  $-0.35$  eV, respectively, compared to the 0% sample, with the onset of absorption reduced due to the Sn alloying in all cases. The shifts here are greater than that expected for this level of Sn alloying<sup>[23]</sup> but are comparable to the redshifts observed for the three CL luminescence bands. Despite the greater Sn content of the TGO/sapphire samples, the comparable magnitude of the absorption shift and CL peak redshifts in Figure 7 reinforces that bandgap reduction is the most probable reason for the observed shift. The unknown impact of strain and band bowing may explain why similar energy shifts are observed despite the differences in Sn content. As previously mentioned, XRD measurements performed on these samples indicate the possibility that  $\alpha$ - or  $\kappa$ - phase material is beginning to form with the larger bandgap of both  $\alpha$ - $\text{Ga}_2\text{O}_3$  and  $\kappa$ - $\text{Ga}_2\text{O}_3$  also complicating the interpretation of the shift in the onset of absorption.

## 4. Conclusion

Here we have characterized a series of MBE-grown  $\text{Ga}_2\text{O}_3$  thin films grown on various substrates. WDX compositional measurements indicate a moderate level of Sn alloying, up to  $x \approx 0.11$ , with growth temperature and substrate choice greatly impacting Sn incorporation. Optical properties were determined through RT cathodoluminescence spectroscopy, indicating there is reduced UV and strong blue luminescence within the layers as gallium vacancies are induced within the film. The formation of  $V_{\text{Ga}}\text{-Sn}$  complexes with these vacancies results in the onset of a green spectral band unseen with  $\text{Ga}_2\text{O}_3$ . Optical behavior was further characterized through simultaneous WDX and CL cross-sectional mapping. A clear redshift of the three distinct spectral luminescence bands was found with shifts of  $\approx 0.3$  eV for UV, blue, and green (for  $x \approx 0.06$ ) as a result of the reduced bandgap. While the CL intensities and peak positions vary for the TGO samples grown on different substrates, the trend of peak shifting for UV, blue, and green emissions is similar for all the TGO samples immaterial of the substrate type. Nonetheless, our CL result shows that as the Sn content increased from  $x = 0.2\%$  to 5.6%, the density of Sn-related defects increased for the TGO samples grown on (010) oriented  $\text{Ga}_2\text{O}_3$  substrate. On the other hand, the CL emission is very similar for TGO with Sn content of  $x = 2.6\%$  grown on (-201)  $\text{Ga}_2\text{O}_3$  substrate and the higher Sn content sample on (010)  $\text{Ga}_2\text{O}_3$ , implying that the (-201) substrate is less preferable for increasing Sn content, while  $V_{\text{Ga}}$ -related defects remain with similar quantity. This result is confirmed by previous studies<sup>[13,25]</sup> focussing on deep UV photodetectors which showed higher dark currents for similar Sn content TGO films on (-201) substrates compared to (010) substrates. A bandgap reduction as a result of the alloying was confirmed by a shift in the onset of absorption through transmission spectroscopy measurements.

## Acknowledgements

The authors acknowledge support from the EPSRC project "Nanoanalysis for Advanced Materials and Healthcare" (EP/K011952/1 and EP/N010914/1), the EPSRC capital award for core equipment (EP/V034995/1) and an EPSRC vacation bursary for OM.

## Conflict of Interest

The authors declare no conflict of interest.

## Data Availability Statement

Data that support the findings of this study are openly available in University of Strathclyde KnowledgeBase at <https://doi.org/10.15129/baf5b819-d79e-429e-89ae-a31614368592>, reference number [60].

## Keywords

cathodoluminescence, gallium oxide, solar-blind photodetectors, tin-gallium oxide

Received: March 15, 2024  
Revised: May 28, 2024  
Published online: July 2, 2024

- [1] H. W. Xue, Q. M. He, G. Z. Jian, S. B. Long, T. Pang, M. Liu, *Nanoscale Res. Lett.* **2018**, *13*, 290.
- [2] D. Shinohara, S. Fujita, *Jpn. J. Appl. Phys.* **2008**, *47*, 7311.
- [3] Z. Alaie, S. M. Nejad, M. H. Yousefi, *Mater. Sci. Semicond. Process.* **2015**, *29*, 16.
- [4] E. V. Gorokhov, A. N. Magunov, V. S. Feshchenko, A. A. Altukhov, *Exp. Tech.* **2008**, *51*, 280.
- [5] H. Chen, K. Liu, L. Hu, A. A. Al-Ghamdi, X. Fang, *Mater. Today.* **2015**, *18*, 493.
- [6] R. Yuan, J. Ma, *China Commun.* **2016**, *13*, 63.
- [7] R. J. Drost, B. M. Sadler, *Semicond. Sci. Technol.* **2014**, *29*, 84006.
- [8] D. Kedar, *Opt. Eng.* **2009**, *48*, 046001.
- [9] M. Higashiwaki, K. Sasaki, A. Kuramata, T. Masui, S. Yamakoshi, *Appl. Phys. Lett.* **2012**, *100*, 13504.
- [10] A. J. Green, J. Speck, G. Xing, P. Moens, F. Allerstam, K. Gumaelius, T. Neyer, A. Arias-Purdue, V. Mehrotra, A. Kuramata, K. Sasaki, S. Watanabe, K. Koshi, J. Blevins, O. Bierwagen, S. Krishnamoorthy, K. Leedy, A. R. Arehart, A. T. Neal, S. Mou, S. A. Ringel, A. Kumar, A. Sharma, K. Ghosh, U. Singiseti, W. Li, K. Chabak, K. Liddy, A. Islam, S. Rajan, et al., *APL Mater.* **2022**, *10*, 029201.
- [11] E. Monroy, F. Calle, J. L. Pau, E. Muñoz, F. Omnès, B. Beaumont, P. Gibart, *J. Cryst. Growth.* **2001**, *230*, 537.
- [12] Q. Cai, H. You, H. Guo, J. Wang, B. Liu, Z. Xie, D. Chen, H. Lu, Y. Zheng, R. Zhang, *Light Sci. Appl.* **2021**, *10*, 2047.
- [13] P. Mukhopadhyay, I. Hatipoglu, Y. K. Frodason, J. B. Varley, M. S. Williams, D. A. Hunter, N. K. Gunasekar, P. R. Edwards, R. W. Martin, F. Wu, A. Mauze, J. S. Speck, W. V. Schoenfeld, *Appl. Phys. Lett.* **2022**, *121*, 111105.
- [14] J. E. N. Swallow, R. G. Palgrave, P. A. E. Murgatroyd, A. Regoutz, M. Lorenz, A. Hassa, M. Grundmann, H. Von Wenckstern, J. B. Varley, T. D. Veal, *ACS Appl. Mater. Interfaces* **2021**, *13*, 2807.
- [15] P. Mukhopadhyay, I. Hatipoglu, T. S. Sakhivel, D. A. Hunter, P. R. Edwards, R. W. Martin, G. Naresh-Kumar, S. Seal, W. V. Schoenfeld, *Adv. Photonics Res.* **2021**, *2*, 2000067.
- [16] C.-C. Wang, S.-H. Yuan, S.-L. Ou, S.-Y. Huang, K.-Y. Lin, Y.-A. Chen, P.-W. Hsiao, D.-S. Wu, *J. Alloys Compd.* **2018**, *765*, 894.
- [17] I. Hatipoglu, P. Mukhopadhyay, F. Alema, T. S. Sakhivel, S. Seal, A. Osinsky, W. V. Schoenfeld, *J. Phys. D: Appl. Phys.* **2020**, *53*, 454001.
- [18] J. Sheng, E. J. Park, B. Shong, J.-S. Park, *ACS Appl. Mater. Interfaces* **2017**, *9*, 23934.
- [19] S. D. Lee, K. Kaneko, S. Fujita, *Jpn. J. Appl. Phys.* **2016**, *55*, 1202B8.
- [20] A. Kuramata, K. Koshi, S. Watanabe, Y. Yamaoka, T. Masui, S. Yamakoshi, *Jpn. J. Appl. Phys.* **2016**, *1202*.
- [21] Y. Li, Y. Li, Y. Ji, H. Wang, D. Zhong, *J. Mater. Sci.* **2022**, *57*, 1186.
- [22] F. Larsson, J. Keller, D. Primetzhofer, L. Riekehr, M. Edoff, T. Törndahl, *J. Vac. Sci. Technol. A.* **2019**, *37*, 030906.
- [23] X. Zhao, W. Cui, Z. Wu, D. Guo, P. Li, Y. An, L. Li, W. Tang, *J. Electron. Mater.* **2017**, *46*, 2366.
- [24] M.-M. Fan, Y.-J. Lu, K.-L. Xu, Y.-X. Cui, L. Cao, X.-Y. Li, *Appl. Surf. Sci.* **2020**, *509*, 144867.
- [25] P. Mukhopadhyay, W. V. Schoenfeld, *J. Vac. Sci. Technol. A.* **2020**, *38*, 013403.
- [26] P. Mukhopadhyay, W. V. Schoenfeld, *Appl. Opt.* **2019**, *58*, D22.
- [27] I. Hatipoglu, D. A. Hunter, P. Mukhopadhyay, M. S. Williams, P. R. Edwards, R. W. Martin, W. V. Schoenfeld, G. Naresh-Kumar, *J. Appl. Phys.* **2021**, *130*, 204501.
- [28] D. Drouin, A. R. Couture, D. Joly, X. Tastet, V. Aimez, R. Gauvin, *Scanning.* **2007**, *29*, 92.
- [29] G. Kusch, F. Mehnke, J. Enslin, P. R. Edwards, T. Wernicke, M. Kneissl, R. W. Martin, *Semicond. Sci. Technol.* **2017**, *32*, 35020.
- [30] P. Gopon, J. Fournelle, P. E. Sobol, X. Llovet, *Microsc. Microanal.* **2013**, *19*, 1698.
- [31] R. W. Martin, P. R. Edwards, K. P. O'Donnell, M. D. Dawson, C. W. Jeon, C. Liu, G. R. Rice, I. M. Watson, *Phys. Status Solidi Appl. Res.* **2004**, *201*, 665.
- [32] T. Degen, M. Sadki, E. Bron, U. König, G. Nénert, in *Powder Diffraction*, Cambridge University Press, Cambridge, UK **2014**: pp. S13.
- [33] S. Nakagomi, Y. Kokubun, *J. Cryst. Growth.* **2012**, *349*, 12.
- [34] M. Kneißl, A. Hassa, D. Splith, C. Sturm, H. Von Wenckstern, T. Schultz, N. Koch, M. Lorenz, M. Grundmann, *APL Mater.* **2019**, *7*, 22516.
- [35] T. Oshima, T. Okuno, S. Fujita, *Jpn. J. Appl. Phys. Part 1 Regul. Pap. Short Notes Rev. Pap.* **2007**, *46*, 7217.
- [36] M. K. Yadav, A. Mondal, S. Das, S. K. Sharma, A. Bag, *J. Alloys Compd.* **2020**, *819*, 153052.
- [37] X. C. Guo, N. H. Hao, D. Y. Guo, Z. P. Wu, Y. H. An, X. L. Chu, L. H. Li, P. G. Li, M. Lei, W. H. Tang, *J. Alloys Compd.* **2016**, *660*, 136.
- [38] C. C. Yen, T. M. Huang, P. W. Chen, K. P. Chang, W. Y. Wu, D. S. Wu, *ACS Omega.* **2021**, *6*, 29149.
- [39] M. Kracht, A. Karg, J. Schörmann, M. Weinhold, D. Zink, F. Michel, M. Rohnke, M. Schowalter, B. Gerken, A. Rosenauer, P. J. Klar, J. Janek, M. Eickhoff, *Phys. Rev. Appl.* **2017**, *8*, 054002.
- [40] M. Higashiwaki, K. Sasaki, A. Kuramata, T. Masui, S. Yamakoshi, *Phys. Status Solidi Appl. Mater. Sci.* **2014**, *211*, 21.
- [41] H. Okumura, M. Kita, K. Sasaki, A. Kuramata, M. Higashiwaki, J. S. Speck, *Appl. Phys. Express.* **2014**, *7*, 95501.
- [42] N. Nepal, D. Scott Katzer, D. J. Meyer, in *Gall Oxide* Elsevier, Amsterdam **2019**, pp. 31–46.
- [43] V. Balakrishnan, *MS Thesis* **2019**, <https://ecommons.cornell.edu/handle/1813/67780> (accessed: June 2022).
- [44] B. W. Krueger, C. S. Dandaneau, E. M. Nelson, S. T. Dunham, F. S. Ohuchi, M. A. Olmstead, *J. Am. Ceram. Soc.* **2016**, *99*, 2467.
- [45] M. Wang, S. Mu, C. G. Van De Walle, *J. Appl. Phys.* **2021**, *130*, 185703.
- [46] W. Mi, X. Du, C. Luan, H. Xiao, J. Ma, *RSC Adv.* **2014**, *4*, 30579.
- [47] Y. Nie, S. Jiao, S. Li, H. Lu, S. Liu, S. Yang, D. Wang, S. Gao, J. Wang, Y. Li, *J. Alloys Compd.* **2022**, *900*, 163431.
- [48] L. Binet, D. Gourier, *J. Phys. Chem. Solids* **1998**, *59*, 1241.
- [49] B. E. Kananen, N. C. Giles, L. E. Halliburton, G. K. Foundos, K. B. Chang, K. T. Stevens, *J. Appl. Phys.* **2017**, *122*, 215703.
- [50] T. Harwig, F. Kellendonk, *J. Solid State Chem.* **1978**, *24*, 255.
- [51] S. I. Maximenko, L. Mazeina, Y. N. Picard, J. A. Freitas, V. M. Bermudez, S. M. Prokes, *Nano Lett.* **2009**, *9*, 3245.
- [52] J. M. Johnson, Z. Chen, J. B. Varley, C. M. Jackson, E. Farzana, Z. Zhang, A. R. Arehart, H. L. Huang, A. Genc, S. A. Ringel, C. G. Van De Walle, D. A. Muller, J. Hwang, *Phys. Rev. X* **2019**, *9*, 041027.
- [53] J. B. Varley, A. Janotti, C. Franchini, C. G. Van De Walle, *Phys. Rev. B - Condens. Matter Mater. Phys.* **2012**, *85*, 81109.
- [54] M. M. Chang, D. Y. Guo, X. L. Zhong, F. B. Zhang, J. B. Wang, *J. Appl. Phys.* **2022**, *132*, 123105.
- [55] Q. D. Ho, T. Frauenheim, P. Deák, *Phys. Rev. B* **2018**, *97*, 115163.
- [56] Y. Usui, D. Nakauchi, N. Kawano, G. Okada, N. Kawaguchi, T. Yanagida, *J. Phys. Chem. Solids* **2018**, *117*, 36.
- [57] A. Kohan, G. Ceder, D. Morgan, C. G. Van De Walle, *Phys. Rev. B - Condens. Matter Mater. Phys.* **2000**, *61*, 15019.
- [58] A. Janotti, C. G. Van De Walle, *Reports Prog. Phys.* **2009**, *72*, 126501.
- [59] M. Karmaoui, A. B. Jorge, P. F. McMillan, A. E. Aliev, R. C. Pullar, J. A. Labrincha, D. M. Tobaldi, *ACS Omega* **2018**, *3*, 13227.
- [60] Data that support the findings of this study are openly available in University of Strathclyde KnowledgeBase at <https://doi.org/10.15129/baf5b819-d79e-429e-89ae-a31614368592>.